Heterostructured Photocatalysts Associating ZnO Nanorods and Ag-In-Zn-S Quantum Dots for the Visible Light-Driven Photocatalytic Degradation of the Acid Orange 7 Dye

Maroua Mrad, Bilel Chouchene, Tahar Ben Chaabane, Thomas Gries, Ghouti Medjahdi, Lavinia Balan, Raphaël Schneider

catalysts

MDPI

Article

Heterostructured Photocatalysts Associating ZnO Nanorods and Ag-In-Zn-S Quantum Dots for the Visible Light-Driven Photocatalytic Degradation of the Acid Orange 7 Dye

Maroua Mrad [1,2], Bilel Chouchene [1], Tahar Ben Chaabane [2], Thomas Gries [3], Ghouti Medjahdi [3], Lavinia Balan [4] and Raphaël Schneider [1,*]

1 Université de Lorraine, CNRS, LRGP, F-54000 Nancy, France
2 Université de Carthage, Faculté des Sciences de Bizerte, LR 18 ES11 Laboratoire des Composés Hétéro-Organiques et des Matériaux Nanostructurés, Jarzouna, Bizerte 7021, Tunisia
3 Université de Lorraine, CNRS, IJL, F-54000 Nancy, France
4 CEMHTI-UPR 3079 CNRS, Site Haute Température, 1D Avenue de la Recherche Scientifique, 45071 Orléans, France
* Correspondence: raphael.schneider@univ-lorraine.fr; Tel.: +33-3-72-74-37-90

Abstract: Heterostructured photocatalysts associating ZnO nanorods (NRs) sensitized by quaternary Ag-In-Zn-S (AIZS) quantum dots (QDs) were prepared by depositing AIZS QDs at the surface of ZnO NRs followed by thermal treatment at 300 °C. The ZnO/AIZS catalysts were characterized by X-ray diffraction, electron microscopy, UV-vis diffuse spectroscopy and by photoelectrochemical measurements. Their photocatalytic activity was evaluated for the bleaching of the Acid Orange 7 (AO7) dye under visible light irradiation. Results show that the association of ZnO NRs with 10 wt% AIZS QDs affords the photocatalyst the highest activity due to the enhanced visible light absorption combined with the improved charge separation. The ZnO/AIZS(10) photocatalyst degrades 98% AO7 in 90 min under visible light illumination, while ZnO NRs can only decompose 11% of the dye. The ZnO/AIZS(10) photocatalyst was also found to be stable and can be reused up to eight times without significant alteration of its activity. This work demonstrates the high potential of AIZS QDs for the development of visible light active photocatalysts.

Keywords: Ag-In-Zn-S quantum dots; heterostructured photocatalyst; photodegradation; visible light; ZnO rods

Citation: Mrad, M.; Chouchene, B.; Ben Chaabane, T.; Gries, T.; Medjahdi, G.; Balan, L.; Schneider, R. Heterostructured Photocatalysts Associating ZnO Nanorods and Ag-In-Zn-S Quantum Dots for the Visible Light-Driven Photocatalytic Degradation of the Acid Orange 7 Dye. *Catalysts* **2022**, *12*, 1585. https://doi.org/10.3390/catal12121585

Academic Editor: Yuanhua Sang

Received: 8 November 2022
Accepted: 1 December 2022
Published: 6 December 2022

1. Introduction

Recently, semiconductor photocatalysis has received a large amount of attention due to its potential to solve both environmental pollution and energy shortage issues. Semiconductor photocatalysis was demonstrated to be effective for the degradation of persistent pollutants in wastewater or for air treatment using inexhaustible solar energy [1–5]. The n-type ZnO semiconductor has been widely applied in photocatalytic degradation due to its low cost, high availability, low toxicity and good chemical stability [6–8]. However, due to its wide bandgap (3.3 eV), ZnO can only be photo-activated by UV light, which accounts only for ca. 4% of the total energy emitted by sunlight. Moreover, the electron-hole pair generated after photo-activation easily recombines, which markedly decreases the photocatalytic efficiency of ZnO.

Among the most promising strategies developed to improve the photoactivity of ZnO is the association with low-bandgap semiconductors or with graphene derivatives to form a heterojunction that allows the reduction in or even inhibition of the recombination of photo-generated electron-hole pairs, and an increase in the optical absorption [9–12]. However, the energy levels of ZnO and of the low bandgap semiconductor must match each other to form the staggered heterojunction.

Quantum dots (QDs) are semiconductor nanocrystals whose bandgap can easily be controlled by varying their size, their composition or their surface chemistry [13,14]. QDs such as CdS, CdSe, PbS and carbon or graphene QDs have been demonstrated to be efficient photosensitizers of ZnO and the heterostructures formed markedly enhance the photocatalytic activity under visible light illumination compared to pure ZnO [15–18]. I-III-VI_2 ternary QDs, such as $CuInS_2$ or $AgInS_2$, are valuable alternatives to the binary QDs previously mentioned and to carbon-based QDs due to their large molar absorption coefficient, their energy bandgap, which matches well with the solar spectrum, and because they contain no toxic element [19,20]. $AgInS_2$ (AIS) QDs and the quaternary Ag-In-Zn-S (AIZS) alloyed QDs obtained after depositing a ZnS shell at their surface were successfully used as photosensitizers and as an electron transport layer to enhance the visible light photoresponse of ZnO or TiO_2 in solar cells [21–25]. Hybrid nanostructured photocatalysts or photoelectrocatalysts composed of AIS nanocrystals or nanosheets and of TiO_2 are also documented in the literature and were successfully used to degrade dyes such as Rhodamine B (RhB), drugs (Docycline, Norfloxacin) and dichlorobenzene, and were also successfully used for bacterial decontamination [26–31]. The use of I-III-VI_2 QDs as photosensitizers of ZnO is far less described. $CuInSe_2$ or $CuInS_2$ QDs were associated to ZnO to engineer visible-light active photocatalysts which were used to decompose dyes such as RhB or AO7 [32–34]. Only one recent report describes the preparation of heterostructured photocatalysts associating ZnO and AIS QDs for phenol degradation and hydrogen photoproduction [35]. Surprisingly, the photosensitizing properties of AIZS QDs to engineer visible light active photocatalysts have never been investigated to date, despite the fact that the energy bandgap of these nanocrystals can more easily be controlled than that of AIS QDs by tuning the Ag/In/Zn/S molar ratio, and the fact that AIZS QDs exhibit a higher photostability than AIS QDs [19,20].

Herein, the first photosensitization of ZnO using AIZS QDs is described. ZnO nanorods (NRs) were prepared via a solvothermal process and decorated with water-dispersible 3-mercaptopropionic acid (MPA)-capped AIZS QDs to engineer visible-light active ZnO/AIZS heterostructured photocatalysts. ZnO NRs were used in this study because one-dimensional (1-D) ZnO nanostructures exhibit an improved photocatalytic activity compared to conventional spherical particles, not only due to their large specific surface area but also because the charge separation is improved in elongated 1-D nanostructures [9,36,37]. The activity of the ZnO/AIZS heterojunctions was evaluated in the photodegradation of the AO7 diazo dye under visible light irradiation. Results show that the association of 10 wt% AIZS QDs with ZnO NRs affords the photocatalyst the highest activity due to the increased optical absorption and enhanced charge separation. Based on the experimental results, the ZnO/AIZS photocatalyst behaves as a type II heterostructure under visible light irradiation [2].

2. Results and Discussion

2.1. ZnO/AIZS Heterojunction Synthesis and Characterization

The synthetic strategy used to assemble ZnO NRs with AIZS QDs is depicted in Scheme 1. Due to the negative charge of MPA-capped AIZS QDs (Zeta potential of -44 ± 3.2 mV at pH 7), the dots strongly bind to the surface of ZnO NRs (Zeta potential of $+27.6 \pm 1.2$ mV at pH 7) via electrostatic attraction, which leads to an intimate contact between ZnO NRs and AIZS QDs. Next, the MPA ligand is decomposed by heating at 300 °C for 5 h, which allows the building of a heterojunction between ZnO and AIZS QDs. The point of zero charge (pzc) of pure ZnO NRs is ca. 9, a value in good accordance with previous reports [38]. A slight decrease in the pzc value is observed after association with AIZS QDs (8.8 and 8.7 for ZnO/AIZS(5) and ZnO/AIZS(10) catalysts, respectively), suggesting the presence of traces of the MPA ligand after thermal treatment at 300 °C for 5 h (Figure S1).

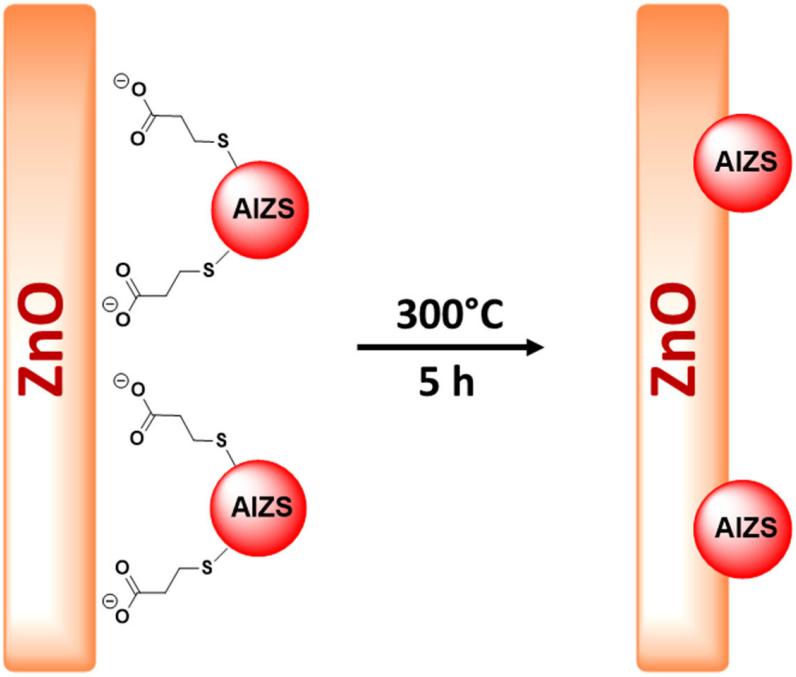

Scheme 1. Schematic representation of ZnO/AIZS photocatalysts' synthesis.

Representative SEM images show that ZnO NRs have an average length up to 500 nm and that their average diameter is ca 17 ± 5 nm (Figure 1a). Upon association with AIZS QDs and heating at 300 °C, an association of these rods in micrometric and more compact structures is observed (Figure 1b). TEM images show that AIZS QDs are well deposited on the surface of ZnO NRs, forming a heterostructure (Figure 1c). Isolated AIZS QDs non-bound to ZnO NRs could not be detected. It is also noteworthy that the size of AIZs QDs increased from ca. 2 nm to ca. 13 nm after the thermal treatment as a result of the decomposition of the MPA capping ligand followed by the coalescence of the nanocrystals. The enlarged HR-TEM image shows lattice spacings of 0.31 and 0.26 nm, belonging to the (111) and (002) crystal planes of cubic AIZS and wurtzite ZnO, respectively, further demonstrating that the heterostructured catalyst was formed (Figure 1d).

The HAADF-STEM image of the ZnO/AIZS(10) photocatalyst and the corresponding elemental mapping images of Zn, O, S, Ag, and In elements further demonstrate the formation of the heterostructured photocalyst and confirm that AIZS QDs are bound to the surface of ZnO NRs (Figure 2).

The photocatalysts were further characterized by X-ray diffraction (Figure 3). AIZS QDs exhibit a cubic structure (JCPDS No. 03-065-9585) and the wide diffraction peaks confirm the small size of the nanocrystals [20,38]. Sharp and intense diffraction peaks can be observed for ZnO NRs, indicating their highly crystalline nature. All diffraction peaks are in good agreement with the hexagonal wurtzite structure of ZnO (JCPDS No. 00-036-1451) and no crystalline impurity can be detected [39]. These results are in good agreement with HR-TEM observations. All reflections observed for ZnO/AIZS catalysts correspond to ZnO. AIZS QDs were not detected by XRD likely due to the weak loading in QDs, as well as their lower crystallinity compared to ZnO. Finally, no impurities were detected, which shows that the ZnO/AIZS heterostructures were successfully prepared.

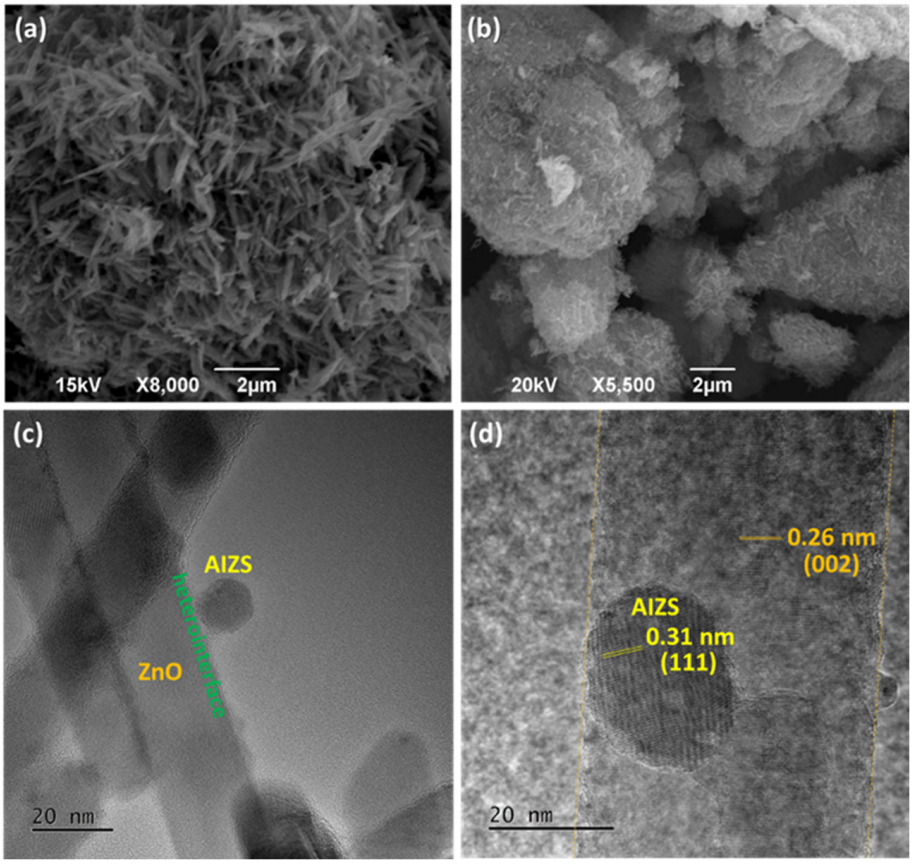

Figure 1. SEM images of (**a**) ZnO NRs and (**b**) the ZnO/AIZS(10) photocatalyst. (**c**) TEM and (**d**) HR-TEM images of the ZnO/AIZS(10) photocatalyst.

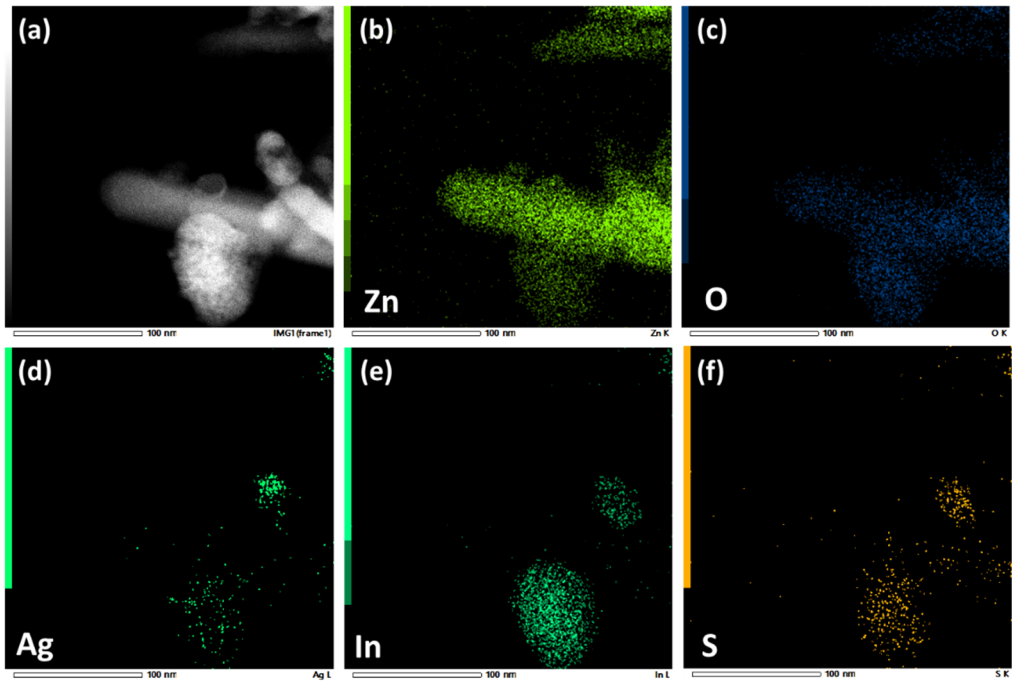

Figure 2. (**a**) High-angle annular dark field (HAADF) STEM images of the ZnO/AIZS(10) heterostructured photocatalyst and the corresponding EDX mapping of (**b**) Zn, (**c**) O, (**d**) Ag, (**e**) In and (**f**) S elements, respectively.

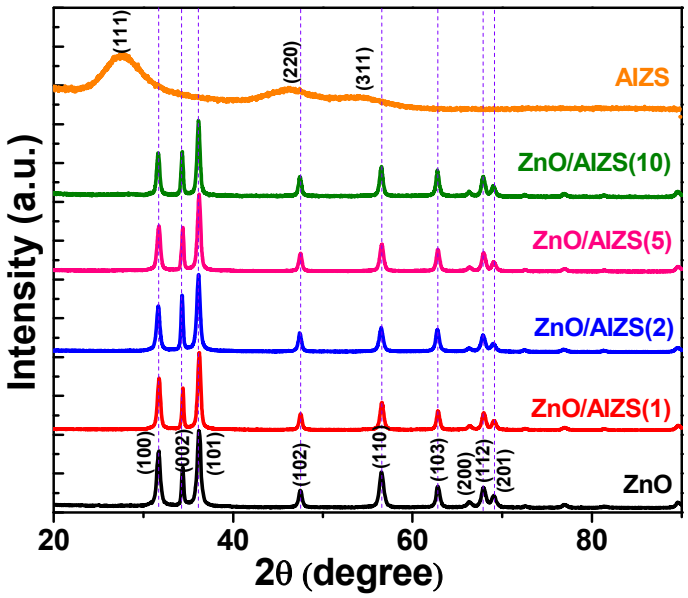

Figure 3. XRD patterns of AIZS QDs, ZnO NRs and ZnO/AIZS heterostructured photocatalysts.

2.2. Optical Properties

The optical properties of ZnO NRs, AIZS QDs and of ZnO/AIZS catalysts were investigated by DRS and the bandgap energies were determined using the Kubelka-Munk equation $(\alpha h\gamma)^n = A\ (h\gamma\text{-}Eg)$, where α is the absorption coefficient, h is the Planck's constant, γ is the light frequency, A is a constant and $n = 2$ for the direct bandgap ZnO semiconductor (Figure 4). Pure ZnO NRs do not absorb in the visible region due to their wide bandgap of 3.19 eV. After thermal treatment at 300 °C, the bandgap of AIZS QDs is 1.99 eV, indicating that the dots may absorb visible light until ca. 623 nm. The heterostructured ZnO/AIZS photocatalysts show enhanced visible light absorption, resulting from the low bandgap of AIZS QDs and from their high visible light absorption capability. The bandgaps determined are 3.17, 3.15, 3.09 and 3.06 eV for ZnO/AIZS(1), ZnO/AIZS(2), ZnO/AIZS(5) and ZnO/AIZS(10) composites, respectively. The improved optical absorption of ZnO/AIZS catalysts should favor the production of electron-hole pairs, and thus improve the photocatalytic performance under visible light irradiation, as described below.

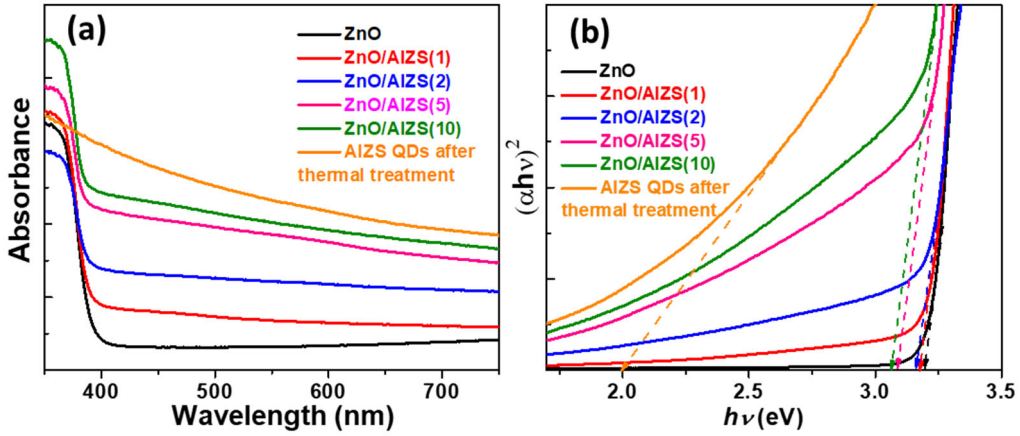

Figure 4. (**a**) UV-visible DRS analyses and (**b**) the estimated bandgap energies of ZnO NRs, AIZS QDs and ZnO/AIZS catalysts.

2.3. Photocatalytic Degradation of OA7 and Kinetic Study

The influence of the ZnO/AIZS photocatalysts' composition on their photocatalytic activity was assessed in the degradation of the OA7 diazo dye (concentration of 10 mg/L) selected as a target pollutant. Experiments were conducted under visible light irradiation ($\lambda > 420$ nm, irradiance of 20 mW/cm^2). As can be seen from Figure 5a, ca. 15% of the dye is adsorbed at the surface of ZnO and ZnO/AIZS catalysts after 30 min of stirring in the dark, while no adsorption could be observed on AIZS QDs. This likely originates from the electrostatic repulsion between the negatively charged OA7 dye at pH 7 and ZnO NRs [40,41], and from residues of the MPA ligand still present at the surface of the AIZS QDs after the thermal treatment at 300 °C. Upon irradiation, a weak photocatalytic activity is observed for AIZS QDs, ZnO NRs, ZnO/AIZS(1) and ZnO/AIZS(2) composites and the degradation does not exceed 11%, likely due to the poor separation ability of electron-hole pairs and to the wide bandgap of these catalysts (see Figure 4). Much better results were obtained when increasing the loading of AIZS QDs at the surface of ZnO NRs, and the degradation reached 49 and 98% for ZnO/AIZS(5) and ZnO/AIZS(10) catalysts, respectively, after 90 min irradiation. These results show that the amount of AIZS QDs associated to ZnO NRs plays a major role in the efficiency of the photogenerated electron-hole separation, which is induced by a sufficient and intimate heterogeneous interface between AIZS QDs and ZnO NRs. Figure 5b shows the evolution of the UV-visible absorption spectra of OA7 during the photocatalytic treatment using the ZnO/AIZS(10) composite, which further confirms the decomposition of the dye.

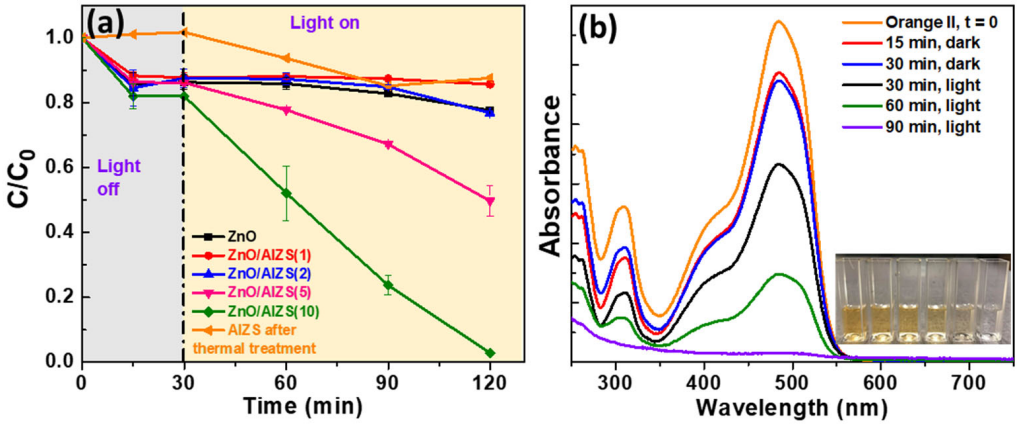

Figure 5. (**a**) Photocatalytic degradation kinetics of OA7 aqueous solution using AIZS QDs, ZnO NRs and ZnO/AIZS heterostructured photocatalysts and (**b**) evolution of UV-visible absorption spectra of AO7 during the photodegradation using the ZnO/AIZS(10) catalyst (the inset of b is a photograph of aliquots taken during the photodegradation).

The photodegradation kinetics were determined using the pseudo-first-order model $\ln(C_0/C_t) = kt$, where C_0 and C_t are the initial concentration and after a time t of OA7, and k is the kinetic constant. The k values determined for AIZS QDs, ZnO NRs, ZnO/AIZS(1), ZnO/AIZS(2), ZnO/AIZS(5) and ZnO/AIZS(10) composites are 0.61x 10^{-3}, 1.17 $\times$ 10^{-3}, 0.26 $\times$ 10^{-3}, 1.40 $\times$ 10^{-3}, 5.99 $\times$ 10^{-3} and 36.27 $\times$ 10^{-3} min^{-1}, respectively, and confirm that the ZnO/AIZS(10) catalyst displays the highest activity (Figure S2).

2.4. Reuse and Stability of the Photocatalyst

The reusability and the stability of the ZnO/AIZS(10) photocatalyst were investigated for the degradation of OA7. As shown in Figure 6a, only a small decrease in the photodegradation yield from 98 to 91% is observed after eight cycles, indicating that the catalyst exhibits a high photostability. The XRD patterns of the starting and of the reused ZnO/AIZS(10) catalysts (Figure 6b) and the corresponding SEM images (Figure S3) show

no change in the crystallinity and in the morphology, further confirming the high stability of the catalyst and its potential for practical photocatalytic applications.

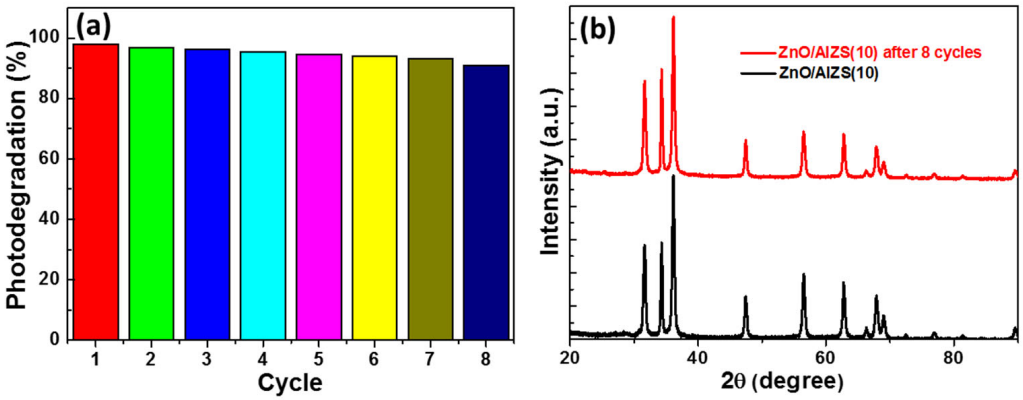

Figure 6. (**a**) Recyclability of the ZnO/AIZS(10) photocatalyst and (**b**) XRD patterns of the native and of the reused ZnO/AIZS(10) catalyst.

2.5. Photocatalytic Mechanism

To investigate the separation, the migration and the recombination of photogenerated electron-hole pairs in ZnO/AIZS catalysts, photoelectrochemical measurements were conducted by depositing the catalysts on FTO glasses and using a bias potential of 0.5 V vs. Ag/AgCl [10]. The photocurrent response of ZnO and ZnO/AIZS photocatalysts was determined during repeated on-off cycles of visible light illumination (Figure 7a). Note that no photocurrent response was detected for AIZS QDs. All ZnO and ZnO/AIZS catalysts show fast photocurrent responses in each light cycle and the response decreases quickly when the light was turned off during the ten cycles of light irradiation. The photocurrent produced by pure ZnO is weak but increases with the loading of AIZS QDs on the surface of ZnO NRs, the highest value being measured for the ZnO/AIZS(10) (ca. 6.8 times higher than that of pure ZnO), which is in good agreement with photocatalytic experiments.

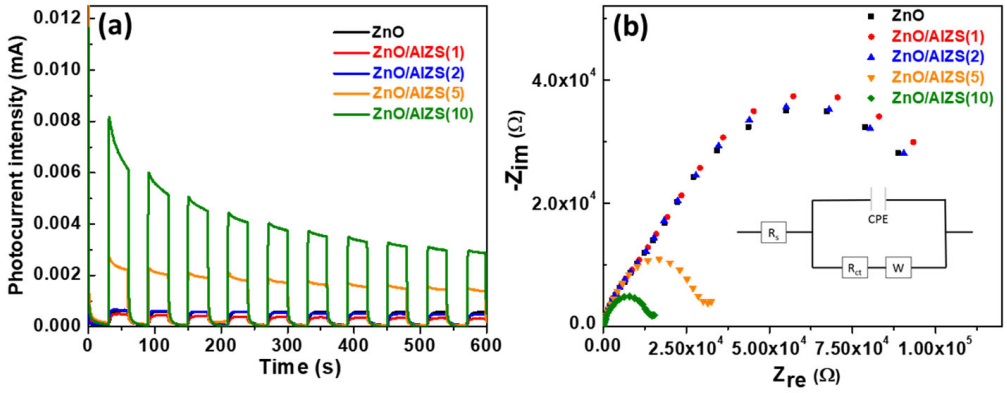

Figure 7. (**a**) Transient photocurrent response and (**b**) EIS Nyquist plots of ZnO and ZnO/AIZS photocatalysts (the inset is the Randles equivalent circuit used for fitting impedance spectra where Rs is the solution resistance, R_{CT} the polarization resistance, W the Warburg impedance and CPE the constant phase element).

The electrochemical impedance spectroscopy (EIS) measurements performed on ZnO and ZnO/AIZS catalysts are described in Figure 7b. The diameter of the semicircular Nyquist plot is the smallest for the ZnO/AIZS(10) composite, which is in good accordance with photocurrent measurements, and further confirms that loading 10 wt% of AIZS QDs onto ZnO NRs allows a decrease in the transfer resistance and thus shows that the charge carriers' recombination in the ZnO/AIZS(10) catalyst is limited compared to the other

samples. From the regression, the charge transfer resistance R_{CT} was determined (see Table S1). As expected by the decrease in the diameter of the semi-circles on Nyquist plots, the decrease in R_{CT} observed with the increase in the AIZS QDs loading confirms that the charge transferability is the highest in the ZnO/AIZS(10) catalyst. This indicates that QDs deposited at the surface of ZnO NRs provide a charge-transfer pathway, via interparticular charge delocalization, for photogenerated electrons.

Scavenging experiments of the active species involved in the photodecomposition of AO7 were also conducted to explore the possible mechanism. For that purpose, *t*-BuOH, benzoquinone (BQ), DMSO, EDTA, NaN_3 and the catalase enzyme were used as scavengers of hydroxyl ($^{\bullet}OH$) radicals, superoxide ($O_2^{\bullet-}$) radicals, electrons (e^-), holes (h^+), singlet oxygen ($^1O_2$) and hydrogen peroxide (H_2O_2), respectively [8,10]. Figure 8 shows that species playing a key role in the degradation of AO7 are holes, hydrogen peroxide and $^{\bullet}OH$ radicals. When adding EDTA, catalase and *t*-BuOH during photocatalytic experiments, the photodegradation falls to 3, 30 and 45%, respectively, after 90 min irradiation. Singlet oxygen and $O_2^{\bullet-}$ radicals are also involved in the decomposition of the dye but to a lesser extent (64 and 67% degradation after 90 min), while the influence of electrons is very low (91% degradation after 90 min).

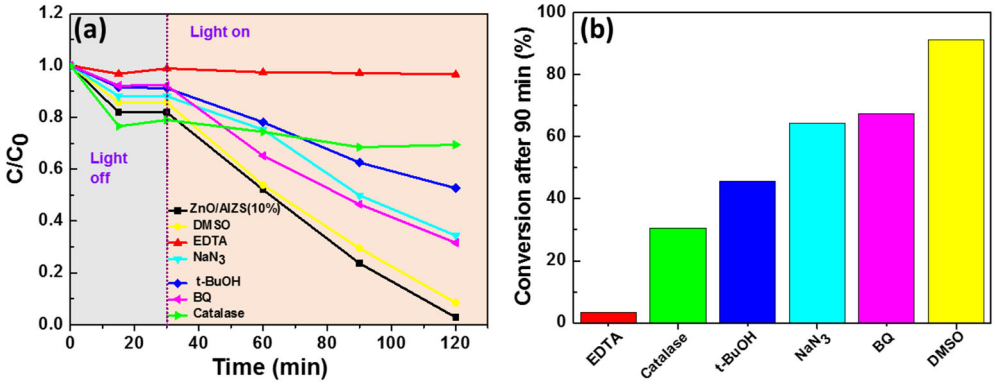

Figure 8. (**a**) Photodegradation of AO7 using the ZnO/AIZS(10) catalyst in the presence of scavengers and (**b**) percentage of AO7 degradation after 90 min of visible light irradiation.

Using UV-visible DRS spectra, the valence band (VB) and the conduction band (CB) potentials of ZnO NRs and AIZS QDs were determined using Formulas (1) and (2):

$$E_{VB} = \chi - E^e + 0.5\,Eg \quad (1)$$

$$E_{CB} = E_{VB} - Eg \quad (2)$$

where E_{VB}, E_{CB} and Eg are the VB potential, the CB potential and Eg is the bandgap (2.47 eV for the ZnO/AIZS(10) composite according to DRS results), respectively, and E^e is the energy of free electrons on the hydrogen scale (ca. 4.5 eV) [42]. The χ values for ZnO and AIZS QDs are 5.89 and 4.95, respectively. The values determined for E_{VB}(ZnO) and E_{CB}(ZnO) are 2.88 and −0.3 eV, respectively, and E_{VB}(AIZS) and E_{CB}(AIZS) are 1.44 and −0.54 eV, respectively. The energy band structure of the ZnO/AIZS catalyst is described in Figure 9a.

Based on the experimental results described above, the following photodegradation mechanism can be proposed (Figure 9b). For the ZnO/AIZS photocatalyst, a typical type-II band alignment is observed, in which the positions of the VB and CB of AIZS QDs are higher than those of ZnO [2]. It is noteworthy that the difference of chemical potential between AIZS QDs and ZnO generates an interfacial band bending. The built-in field thus generated drives photogenerated electrons located in the CB of AIZS QDs after visible irradiation to move to the CB of ZnO and thus enhances the spatial separation and the lifetime of charge carriers. The electrons located in the CB of ZnO reduce O_2 into $O_2^{\bullet-}$ radicals, which were shown to play an important role in the bleaching of the dye. The

holes in the VB of AIZS QDs play a major role in the decomposition of OA7 and may either directly oxidize the dye (AO7 → $AO7^+$) and/or reduce $O_2^{\bullet -}$ radicals into $^3O_2$ and $^1O_2$, the latter species also being involved in the photodegradation.

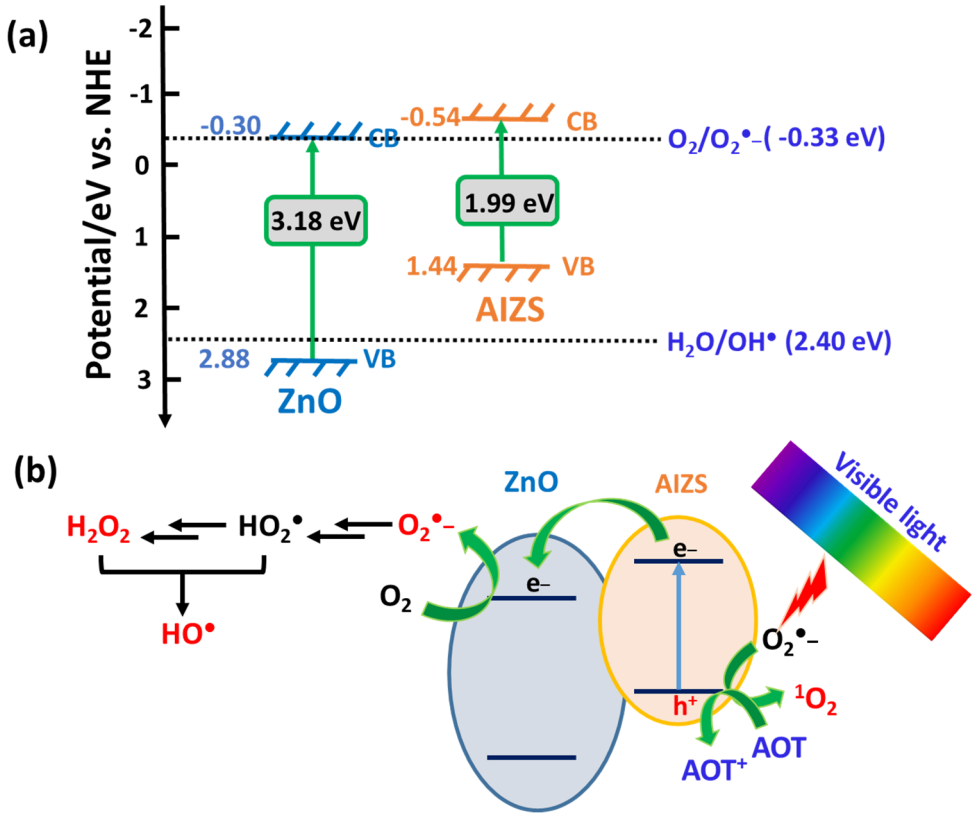

Figure 9. (**a**) Energy band positions of AIZS QDs and ZnO NRs and (**b**) mechanism of the visible light-driven photodegradation of AO7 using the ZnO/AIZS(10) photocatalyst.

Hydrogen peroxide is likely produced by the protonation of $O_2^{\bullet -}$ radicals followed by their reduction (reactions (3) and (4)).

$$O_2^{\bullet -} + H_2O \rightarrow HO_2^{\bullet} + HO^- \quad (3)$$

$$HO_2^{\bullet} + H_2O \rightarrow H_2O_2 + {}^{\bullet}OH \quad (4)$$

The key role played by H_2O_2 in the oxidation of the dye was demonstrated by the addition of the catalase enzyme which decomposes H_2O_2 and thus strongly inhibits the photodegradation (reaction (5)) [43].

$$2\,H_2O_2 \xrightarrow{\text{Catalase}} 2\,H_2O + O_2 \quad (5)$$

The VB potential of AIZS QDs (+1.44 eV vs. NHE) is higher than the potential of the $H_2O/{}^{\bullet}OH$ couple (+2.40 eV vs. NHE), indicating that holes cannot oxidize H_2O and produce $^{\bullet}OH$ radicals, which are the species primarily involved in photodegradation. We assume that these radicals may be produced by a reaction of the $HO_2^{\bullet}$ radical with H_2O (reaction (4)), reduction of H_2O_2 (reaction (6)), reaction of H_2O_2 with $O_2^{\bullet -}$ radicals (reaction (7)) or by the decomposition of H_2O_2 under visible light irradiation (reaction (8)).

$$H_2O_2 + e^- \rightarrow {}^{\bullet}OH + HO^- \quad (6)$$

$$H_2O_2 + O_2^{\bullet -} \rightarrow {}^{\bullet}OH + HO^- + O_2 \quad (7)$$

$$H_2O_2 \rightarrow 2\,{}^{\bullet}OH \quad (8)$$

3. Materials and Methods

3.1. Materials and Instruments

$Zn(OAc)_2 \bullet 2H_2O$ (Sigma), NaOH (Sigma), Acid Orange 7 (AO7, Sigma), tert-butanol (Sigma), benzoquinone (Sigma), ethylenediaminetetraacetic acid disodium salt dihydrate (Fisher), sodium azide (Sigma), catalase (Sigma), DMSO (Fisher) and ethanol (VWR) were of analytical grade and used as obtained. MPA-capped AIZS QDs with a Ag/In molar ratio of 1/5 were prepared in aqueous phase according the synthetic protocol recently reported [20].

The structure of the photocatalysts was investigated by powder X-ray diffraction (XRD) using a Panalytical X'Pert pro MPD diffractometer with Cu Kα radiation. The morphology of the photocatalysts was studied using scanning electron microscopy (SEM) performed on JEOL JSM-6490 LV and JEOL JSM IT800 instruments. Transmission electron microscopy (TEM) images were taken using Philips CM200 equipment operating at an acceleration voltage of 200 kV. A high-resolution TEM (HR-TEM, JEOL ARM200F) was used to acquire the high angle annular dark field-scanning transmission electron microscopy (HAADF-STEM) image and the EDS mapping of the samples (a 68–174.5 mrad inner-outer collection angle and a 0.1 nm probe size were used).

The Zeta potential of the catalysts was measured using a Malvern Zetasizer Nano ZS equipment.

UV-visible absorption spectra were recorded on a Thermo Scientific Evolution 220 spectrometer. UV-visible spectra diffuse reflectance spectra (DRS) of powders were measured using a Shimadzu 2600–2700 spectrometer.

The photoelectrochemical measurements were performed in a 0.1 M Na_2SO_4 aqueous solution on a SP150 Bio-Logic potentiostat connected to a three-electrode cell (with a Pt wire as counter electrode, a saturated Ag/AgCl reference electrode and FTO glass substrates (1 cm^2) coated with ZnO or ZnO/AIZS particles as the working electrode). The photocurrent density was evaluated from chronoamperometric measurements by applying a positive potential of +0.5 V vs. Ag/AgCl. Electrochemical impedance spectroscopy (EIS) was performed at open circuit with a magnitude of the modulation signal of 10 mV in a frequency range of 500 kHz to 10 mHz. The impedance spectra were fitted by a Randles equivalent circuit including a solution resistance R_S, a constant phase element (CPE), charge transfer resistance R_{CT} and a Warburg impedance W.

3.2. Solvothermal Synthesis of ZnO NRs

ZnO rods were prepared by hydrolysis of $Zn(OAc)_2$ under solvothermal conditions. Briefly, $Zn(OAc)_2 \bullet 2H_2O$ (511 mg) was added to 35 mL ethanol and the mixture was stirred until complete dissolution. A solution of NaOH (466 mg) in 35 mL ethanol was dropwise added to $Zn(OAc)_2$ and the mixture was allowed to react for 30 min at room temperature to form the ZnO nuclei. Next, the solution was poured into a 100 mL Teflon-sealed autoclave and heated at 160 °C for 24 h. After the solution was naturally cooled to room temperature, ZnO rods were recovered by centrifugation, washed with water (2 × 20 mL), with ethanol (2 × 20 mL), and finally dried at 50 °C overnight (ca. 150 mg of ZnO NRs are obtained).

3.3. Synthesis of ZnO/AIZS Photocatalysts

A representative synthesis of ZnO/AIZS(5) is described. To MPA-capped AIZS QDs (5 mg) dispersed in water at pH 7 were added 95 mg of ZnO NRs and the solution was stirred for 1 h at 20 °C before being sonicated for 10 min. Water was then removed by heating at 70 °C for 24 h. Finally, the powder was calcinated in air at 300 °C for 5 h with a heating rate of 2 °C/min, and the heterostructured ZnO/AIZS catalyst obtained was used without further treatment. Other ZnO/AIZS photocatalysts were prepared using the same synthetic protocol but by varying the ZnO to AIZS QDs mass ratio (1, 2, 5 or 10 wt% AIZS QDs relative to ZnO NRs).

3.4. Photocatalytic Tests

The photodegradation of AO7 (concentration of 10 mg/L) was conducted in a batch reactor. An Osram Ultra Vitalux lamp fitted with an UV cutoff filter (>420 nm) was used as light source (the light irradiance at the surface of the OA7 solution was fixed at 20 mW/cm^2). In a typical reaction, 30 mg of the catalyst and 30 mL of the OA7 solution were placed in the reactor and the mixture was sonicated for 2 min in the dark. Before irradiation, the mixture was further magnetically stirred for 30 min in the dark to reach the adsorption/desorption equilibrium. At given intervals (15 or 30 min), aliquots (2 mL) were removed, centrifuged (15,000 rpm for 2 min) to separate the catalyst and analyzed by UV-visible spectroscopy. Blank experiments in the absence of catalyst or light irradiation confirmed that the degradation of the dye could only be observed in the presence of the ZnO/AIZS catalyst and under light illumination.

Scavenging experiments were performed to identify the species involved in the photodegradation process. These experiments were conducted using *tert*-butanol (*t*-BuOH, 10 mM), benzoquinone (BQ, 10 mM), DMSO (10 mM), ethylenediaminetetraacetic acid disodium salt dihydrate (EDTA, 10 mM), sodium azide (NaN_3, 10 mM) and catalase (28,600 U) as scavengers of $^{\bullet}OH$ and $O_2^{\bullet-}$ free radicals, electrons and holes, singlet oxygen $^1O_2$, and H_2O_2, respectively.

4. Conclusions

In summary, novel ZnO/AIZS heterostructured photocatalysts were prepared through the association of ZnO NRs with AIZS QDs under sonication followed by thermal treatment at 300 °C. The ZnO/AIZS(10) catalyst exhibits the highest activity for the AO7 dye photodegradation due to the enhanced visible light absorption and to the type II heterojunction between ZnO NRs and AIZS QDs, which promotes the charge separation upon photoactivation. Our study demonstrates the high potential of AIZS QDs as a photosensitizer of wide bandgap semiconductors such as ZnO, and should not only find applications in emerging pollutant photodegradation but also in other photocatalytic processes linked to energy production.

Supplementary Materials: The following supporting information can be downloaded at: https://www.mdpi.com/article/10.3390/catal12121585/s1, Figure S1: Zeta potentials of ZnO NRs, ZnO/AIZS(5) and ZnO/AIZS(10) heterostructured photocatalysts as a function of pH; Figure S2: Plots of $\ln(C_0/C)$ for the determination of the first-order rate constants k of the photodegradation of Orange II under visible light irradiation; Figure S3: SEM images of (**a**) the as-prepared and (**b**) the reused ZnO/AIZS(10) photocatalyst; Table S1: Impedance parameters obtained after fitting the EIS curves with the Randles equivalent model, where n is the exponent of the constant phase element Q and σ is the Warburg coefficient.

Author Contributions: Conceptualization, T.B.C. and R.S.; methodology, M.M. and B.C.; validation, T.B.C., T.G., L.B., G.M. and R.S.; formal analysis, M.M. and B.C.; investigation, M.M., G.M. and B.C.; data curation, T.G., G.M. and L.B.; writing—original draft preparation, M.M. and B.C.; writing—review and editing, R.S.; supervision, T.B.C. and R.S.; project administration, T.B.C. and R.S.; funding acquisition, R.S. All authors have read and agreed to the published version of the manuscript.

Funding: This research received no external funding.

Data Availability Statement: Not applicable.

Acknowledgments: This project has benefited from the expertise and the facilities of the Platform MACLE-CVL, which was co-funded by the European Union and Centre-Val de Loire Region (FEDER).

Conflicts of Interest: The authors declare no conflict of interest.

References

1. Kabra, K.; Chaudhary, R.; Sawhney, R.L. Treatment of hazardous organic and inorganic compounds through aqueous-phase photocatalysis: A Review. *Ind. Eng. Chem. Res.* **2004**, *43*, 7683–7696. [CrossRef]
2. Wang, Y.; Wang, Q.; Zhan, X.; Wang, F.; Sadfar, M.; He, J. Visible light driven type II heterostructures and their enhanced photocatalysis properties: A review. *Nanoscale* **2013**, *5*, 8326–8339. [CrossRef] [PubMed]
3. Rueda-Marquez, J.J.; Levchuk, I.; Fernandez-Ibanez, P.; Sillanpaa, M. A critical review on application of photocatalysis for toxicity reduction of real wastewaters. *J. Clean. Prod.* **2020**, *258*, 120694. [CrossRef]
4. Nabeel Ahmed, S.; Haider, W. Heterogeneous photocatalysis and its potential applications in water and wastewater treatment: A review. *Nanotechnology* **2018**, *29*, 342001. [CrossRef] [PubMed]
5. Shafiq, I.; Hussain, M.; Shehzad, N.; Maafa, I.M.; Akhter, P.; Amjad, U.-e.s.; Shafique, S.; Razzaq, A.; Yang, W.; Tahir, M.; et al. The effect of crystals facets and induced porosity on the performance of monoclinic $BiVO_4$ for the enhanced visible-light driven photocatalytic abatement of methylene blue. *J. Environ. Chem. Eng.* **2019**, *7*, 103265. [CrossRef]
6. Lee, K.M.; Lai, C.W.; Ngai, K.S.; Juan, J.C. Recent developments of zinc oxide based photocatalyst in water treatment technology: A review. *Water. Res.* **2016**, *88*, 428–448. [CrossRef]
7. Goktas, S.; Goktas, A. A comparative study on recent progress in efficient ZnO based nanocomposite and heterojunction photocatalysts: A review. *J. Alloys Compd.* **2021**, *863*, 158734. [CrossRef]
8. Moussa, H.; Girot, E.; Mozet, K.; Alem, H.; Medjahdi, G.; Schneider, R. ZnO rods/reduced graphene oxide composites prepared via a solvothermal reaction for efficient sunlight-driven photocatalysis. *Appl. Catal. B Environ.* **2016**, *185*, 11–21. [CrossRef]
9. Eley, C.; Li, T.; Liao, F.; Fairclough, S.M.; Smith, J.M.; Smith, G.; Edman Tsang, S.C. Nanojunction-mediated photocatalytic enhancement in heterostructured CdS/ZnO, CdSe/ZnO, and CdTe/ZnO nanocrystals. *Angew. Chem.* **2014**, *126*, 7972–7976. [CrossRef]
10. Moussa, H.; Chouchene, B.; Gries, T.; Balan, L.; Mozet, K.; Medjahdi, G.; Schneider, R. Growth of ZnO nanorods on graphitic carbon nitride gCN sheets for the preparation of photocatalysts with high visible-light activity. *ChemCatChem* **2018**, *10*, 4987–4997. [CrossRef]
11. Yaqoob, A.A.; Mohr Noor, N.H.b.; Umar, K.; Adnan, R.; Mohamad Ibrahim, M.N.; Rashid, M. Graphene oxide-ZnO nanocomposite: An efficient visible light photocatalyst for degradation of rhodamine B. *Appl. Nanosci.* **2021**, *11*, 1291–1302. [CrossRef]
12. Oliveira, M.C.; Fonseca, V.S.; Andrade Neto, N.F.; Ribeiro, R.A.P.; Longo, E.; De Lazaro, S.R.; Motta, F.V.; Bomio, M.R.D. Connecting theory with experiment to understand the photocatalytic activity of CuO–ZnO heterostructure. *Ceram. Int.* **2020**, *46*, 9446–9454. [CrossRef]
13. Bera, D.; Qian, L.; Tseng, T.K.; Holloway, P.H. Quantum dots and their multimodal applications: A Review. *Materials* **2010**, *3*, 2260–2345. [CrossRef]
14. García de Arquer, F.P.; Talapin, D.V.; Klimov, V.I.; Arakawa, Y.; Bayer, M.; Sargent, E.H. Semiconductor quantum dots: Technological progress and future challenges. *Science* **2021**, *373*, eaaz8541. [CrossRef] [PubMed]
15. Gao, G.; Xi, Q.; Zhou, H.; Zhao, Y.; Wu, C.; Wang, L.; Guo, P.; Xu, J. Selectivity of quantum dot sensitized ZnO nanotube arrays for improved photocatalytic activity. *Phys. Chem. Chem. Phys.* **2017**, *19*, 11366–11372. [CrossRef] [PubMed]
16. Qu, Y.; Xu, X.; Huang, R.; Qi, W.; Su, R.; He, Z. Enhanced photocatalytic degradation of antibiotics in water over functionalized N,S-doped carbon quantum dots embedded ZnO nanoflowers under sunlight irradiation. *Chem. Eng. J.* **2016**, *382*, 123016. [CrossRef]
17. Majunder, T.; Dhar, S.; Dabnath, K.; Prakash Mondal, S. Role of S, N co-doped graphene quantum dots as a green photosensitizer with Ag-doped ZnO nanorods for improved electrochemical solar energy conversion. *Mater. Res. Bull.* **2017**, *93*, 214–222. [CrossRef]
18. Mahmoodi, N.M.; Karimi, B.; Mazarji, M.; Moghtaderi, H. Cadmium selenide quantum dot-zinc oxide composite: Synthesis, characterization, dye removal ability with UV irradiation, and antibacterial activity as a safe and high-performance photocatalyst. *J. Photochem. Photobiol. B Biol.* **2018**, *188*, 19–27. [CrossRef]
19. Berends, A.C.; Mangnus, M.J.J.; Xia, C.; Robouw, F.T.; De Mello Donega, C. Optoelectronic properties of ternary I–III–VI_2 semiconductor nanocrystals: Bright prospects with elusive origins. *J. Phys. Chem. Lett.* **2019**, *10*, 1600–1616. [CrossRef]
20. Mrad, M.; Ben Chaabane, T.; Rinnert, H.; Balan, L.; Jasniewski, J.; Medjahdi, G.; Schneider, R. Aqueous synthesis for highly emissive 3-mercaptopropionic acid-capped AIZS quantum dots. *Inorg. Chem.* **2020**, *59*, 6220–6231. [CrossRef]
21. Han, J.; Liu, Z.; Guo, K.; Ya, J.; Zhao, Y.; Zhang, X.; Hong, T.; Liu, T.J. High-efficiency $AgInS_2$-modified ZnO nanotube array photoelectrodes for all-solid-state hybrid solar cells. *ACS Appl. Mater. Interfaces* **2014**, *6*, 17119–17125. [CrossRef] [PubMed]
22. Sasamura, T.; Okazaki, K.I.; Tsunoda, R.; Kudo, A.; Kuwabata, S.; Torimoto, T. Immobilization of ZnS–$AgInS_2$ solid solution nanoparticles on ZnO rod array electrodes and their photoresponse with visible light irradiation. *Chem. Lett.* **2010**, *39*, 619–621. [CrossRef]
23. Kaewprajak, A.; Kumnorkaew, P.; Sagawa, T. Improved photovoltaic performance and device stability of planar heterojunction perovskite solar cells using TiO_2 and TiO_2 mixed with $AgInS_2$ quantum dots as dual electron transport layers. *Org. Electron.* **2019**, *69*, 26–33. [CrossRef]
24. Kobosko, S.M.; Jara, D.H.; Kamat, P.V. AgInS2–ZnS quantum dots: Excited state interactions with TiO_2 and photovoltaic performance. *ACS Appl. Mater. Interfaces* **2017**, *9*, 33379–33388. [CrossRef]

25. Kaewprajak, A.; Kumnorkaew, P.; Sagawa, T. Silver–indium–sulfide quantum dots in titanium dioxide as electron transport layer for highly efficient and stable perovskite solar cells. *J. Mater. Sci. Mater. Electron.* **2019**, *30*, 4041–4055. [CrossRef]
26. Ganguly, P.; Mathew, S.; Clarizia, L.; Kumar, R.S.; Akande, A.; Hinder, S.J.; Breen, A.; Pillai, S.C. Ternary metal chalcogenide heterostructure ($AgInS_2$–TiO_2) nanocomposites for visible light photocatalytic applications. *ACS Omega* **2020**, *5*, 406–421. [CrossRef]
27. Zhang, M.; Li, X.; Zhao, Q.; Fan, S.; Jiang, Z.; Chen, G. $AgInS_2$ nanoparticles modified TiO_2 nanotube array electrodes: Ultrasonic-assisted SILAR preparation and mechanism of enhanced photoelectrocatalytic activity. *Mol. Catal.* **2017**, *442*, 97–106. [CrossRef]
28. Sun, M.; Chen, Z.; Li, J.; Hou, J.; Xu, F.; Xu, L.; Zeng, R. Enhanced visible light-driven activity of TiO_2 nanotube array photoanode co-sensitized by "green" $AgInS_2$ photosensitizer and In_2S_3 buffer layer. *Electrochim. Acta* **2018**, *269*, 429–440. [CrossRef]
29. Liu, B.; Li, X.; Zhao, Q.; Ke, J.; Tadé, M.; Liu, S. Preparation of $AgInS_2/TiO_2$ composites for enhanced photocatalytic degradation of gaseous o-dichlorobenzene under visible light. *Appl. Catal. B Environ.* **2016**, *185*, 1–10. [CrossRef]
30. Yang, M.; Yan, Y.; Liu, E.; Fan, J.; Hu, X. Ligand and hard base assisted preparation of $AgInS_2$ single phase nanocrystals for enhancing the photocatalytic activity of TiO_2. *J. Phys. D Appl. Phys.* **2021**, *54*, 375101. [CrossRef]
31. Du, J.; Ma, S.; Liu, H.; Fu, H.; Li, L.; Li, Z.; Li, Y.; Zhou, J. Uncovering the mechanism of novel $AgInS_2$ nanosheets/TiO_2 nanobelts composites for photocatalytic remediation of combined pollution. *Appl. Catal. B Environ.* **2019**, *259*, 118062. [CrossRef]
32. Shen, F.; Que, W.; He, Y.; Yuan, Y.; Yin, X.; Wang, G. Enhanced photocatalytic activity of ZnO microspheres via hybridization with $CuInSe_2$ and $CuInS_2$ Nanocrystals. *ACS Appl. Mater. Interfaces* **2012**, *4*, 4087–4092. [CrossRef] [PubMed]
33. Xu, T.; Hu, J.; Yang, Y.; Que, W.; Yin, X.; Wu, H.; Chen, L. Ternary system of ZnO nanorods/reduced graphene oxide/$CuInS_2$ quantum dots for enhanced photocatalytic performance. *J. Alloys Compd.* **2018**, *734*, 196–203. [CrossRef]
34. Donat, F.; Corbel, S.; Alem, H.; Pontvianne, S.; Balan, L.; Medjahdi, G.; Schneider, R. ZnO nanoparticles sensitized by $CuInZn_xS_{2+x}$ quantum dots as highly efficient solar light driven photocatalysts. *Beilstein J. Nanotechnol.* **2017**, *8*, 1080–1093. [CrossRef] [PubMed]
35. Nevarez Martinez, M.C.; Bajorowicz, B.; Klimczuk, T.; Zak, A.; Luczak, J.; Lisowski, W.; Zaleska-Medynska, A. Synergy between $AgInS_2$ quantum dots and ZnO nanopyramids for photocatalytic hydrogen evolution and phenol degradation. *J. Hazard. Mater.* **2020**, *398*, 123250. [CrossRef]
36. Zhang, X.; Qin, J.; Xue, Y.; Yu, P.; Zhang, B.; Wang, L.; Liu, R. Effect of aspect ratio and surface defects on the photocatalytic activity of ZnO nanorods. *Sci. Rep.* **2014**, *4*, 4596. [CrossRef]
37. Leelavathi, A.; Madras, G.; Ravishankar, N. Origin of enhanced photocatalytic activity and photoconduction in high aspect ratio ZnO nanorods. *Phys. Chem. Chem. Phys.* **2013**, *15*, 10795–10802. [CrossRef]
38. McIntyre, G.J.; Moss, G.; Barnea, Z. Anharmonic temperature factors of zinc selenide determined by X-ray diffraction from an extended-face crystal. *Acta Cryst.* **1980**, *A36*, 482–490. [CrossRef]
39. Abrahams, S.C.; Bernstein, J.L. Remeasurement of the structure of hexagonal ZnO. *Acta Cryst.* **1969**, *B25*, 1233–1237. [CrossRef]
40. Mohd Omar, F.; Abdul Aziz, H.; Stoll, S. Stability of ZnO nanoparticles in solution: Influence of pH, dissolution, aggregation and disaggregation effects. *J. Colloid Sci. Biotechnol.* **2014**, *3*, 75–84. [CrossRef]
41. Oakes, J.; Gratton, P. Kinetic investigations of azo dye oxidation in aqueous media. *J. Chem. Soc. Perkin Trans.* **1998**, *2*, 1857–1864. [CrossRef]
42. Xu, Y.; Schoonen, M.A.A. The absolute energy positions of conduction and valence bands of selected semiconducting minerals. *Am. Mineral.* **2000**, *85*, 543–556. [CrossRef]
43. Gao, M.; Ng, T.W.; An, T.; Li, G.; Yip, H.Y.; Zhao, H.; Wong, P.K. The role of catalase and H_2O_2 in photocatalytic inactivation of Escherichia coli: Genetic and biochemical approaches. *Catal. Today* **2016**, *266*, 205–211. [CrossRef]